NIPPON STEEL TECHNICAL REPORT No. 136 JULY 2026

Technical Report

Nanoscopic Reduction Mechanism of Hematite Particle by Hydrogen Revealed via X-ray Spectromicroscopy

Toru TAKAYAMA*
Yasuhiro NIWA
Reiko MURAO
Kazuya FUJINO
Masao KIMURA
Yasuo TAKEICHI
Shoji USHIO
Takashi IIJIMA

Abstract

To reveal the hydrogen reduction mechanism of iron ore, XAFS-CT and synchrotron nano X-ray CT were employed to observe the heterogenous microstructure of the hematite particles after isothermal reduction. These observations are conducted in a non-destructive manner with three dimensional and spatial resolution better than 50 nm. XAFS-CT provided highly accurate three-dimensional valence phase distributions by performing linear combination fitting of X-ray absorption spectra for each voxel, determining the iron chemical states: Fe^{3+}, Fe^{2+}, Fe^{0}. Then, synchrotron nano X-ray CT enabled the phase and pore three-dimensional distinction more quickly. These analyses revealed that topochemical reactions dominated at 973 K, whereas topotaxial reactions prevailed at 1173 K during the initial stage of the reduction. This suggests that differences in the early reduction behavior significantly influence subsequent phase transformations and final reduction fractions. This method is expected to be widely applicable for three-dimensional analysis of materials involving changes in chemical states.

1. Introduction

The steel industry is actively engaged in a wide range of initiatives aimed at the realization of carbon-neutral (CN) steelmaking in order to reduce CO_2 emissions. Among these efforts, hydrogen-based iron ore reduction processes have been identified as one of the most promising technological approaches. When employed as a reducing agent, hydrogen exhibits a higher effective diffusion rate and faster reduction kinetics, compared with carbon monoxide (CO). Therefore, the accelerated development of hydrogen-based reduction technologies necessitates a thorough understanding of the hydrogen reduction mechanisms and behaviors of iron ore.

Previous studies have demonstrated that the reduction of iron oxide (Fe_2O_3) to FeO within iron ore proceeds via a topochemical reaction mechanism and that, as reduction progresses, the reaction behavior is governed by oxygen diffusion within the mineral phase.[1, 2] In addition, it has been reported that the hydrogen reduction of Fe_2O_3 exhibits stagnation at temperatures above 973 K,[3] and it has been suggested that the formation of a dense metallic Fe layer on the particle surface during the reduction process restricts hydrogen diffusion, thereby suppressing further reduction.[4]

Furthermore, it has been suggested that the hydrogen reduction process of hematite (Fe_2O_3) particles involves highly heterogeneous reactions with respect to both microstructural evolution and chemical state.[5, 6] Therefore, high-spatial resolution, three-dimensional, and non-destructive observation techniques are required to elucidate the reduction mechanism in detail. X-ray computed tomography (X-ray CT) represents a powerful tool for three-dimensional, non-destructive microstructural characterization. However, even state-of-the-art laboratory-based cone-beam X-ray CT systems are limited to a spatial resolution of approximately 1 μm at best, which is insufficient for quantitatively evaluating the microstructural evolution of hematite during hydrogen reduction.

On the other hand, recent advances in synchrotron radiation technology have led to the development of synchrotron nano X-ray computed tomography (nano X-CT). This technique enabled by significant improvements in X-ray optical elements, allows for the vi-

* Senior Researcher, Materials Characterization Research Lab., Advanced Technology Research Laboratories
20-1 Shintomi, Futtsu City, Chiba Pref. 293-8511

sualization of three-dimensional structures at high spatial resolution on the order of several tens of nanometers.[7–10] Furthermore, the combination of this technique with X-ray absorption spectroscopy enables the development of "XAFS-CT," which is a measurement technique capable of non-destructively providing three-dimensional chemical state distributions of materials with nanometer-scale spatial resolution and revealing their inherent chemical and structural inhomogeneities.[11–17] XAFS (X-ray Absorption Fine Structure) denotes the fine oscillatory structure observed near the absorption edge of the target element in the X-ray absorption spectrum. This originates from the interference effects associated with the scattering of photoelectrons, emitted from absorbing atoms by neighboring atoms. Analysis of XAFS yields information on the valence state and local structure including coordination number and interatomic distance of the target element.

Therefore, in this study, hematite particles with sizes on the order of tens of micrometers were subjected to hydrogen reduction at different temperatures and times. These particles were then characterized at high spatial resolution (approximately 50 nm) using synchrotron radiation nano X-ray CT and XAFS-CT. This enabled elucidation of the three-dimensional microstructure of the hematite particles and the distribution of the Fe chemical states, thereby enabling a detailed investigation of the hydrogen reduction mechanism.[18]

Specifically, for hematite particles reduced under isothermal conditions at 973 K or 1 173 K for various reaction time conditions, we analyzed the evolution of mineral phases formed during reduction, changes in particle shape, and the microstructure of pores and cracks to investigate the reduction reaction mechanism.[18]

2. Experiments

2.1 Sample preparation and reduction reaction measurement

This study employed a dense hematite fine ore from Brazil (T.Fe: 68.2 mass%, FeO: 0.26 mass%, SiO_2: 2.16 mass%, Al_2O_3: 0.25 mass%, combined water: 0.41 mass%, and average particle size: 60 μm). The hematite particles in this iron ore consist predominantly of single crystals of Fe_2O_3, and the gangue primarily consists of discrete quartz particles. The particles also exhibit a low degree of shape variability.

The above hematite iron ore (15 mg) was subjected to hydrogen reduction using a thermogravimetric analysis (TG) instrument under isothermal conditions at 973 K and 1 173 K. The sample was initially heated to the target temperature at a heating rate of 10 K/min in nitrogen gas with a flow rate of 0.2 NL/min and subsequently held at that temperature for 5 min to stabilize its mass. A reducing gas mixture of H_2/N_2=25/75 (volume ratio) was introduced, and the thermogravimetric measurements were started. To examine microstructural changes during hydrogen reduction, the reducing gas was replaced with nitrogen gas, and the samples were maintained at the same temperature for 5 minutes prior to subsequent cooling under ambient conditions. The reduction times were set to 1 min, 14 min, and 60 min at 973 K, and 1 min, 7 min, and 60 min at 1 173 K where the initial and intermediate times at each temperature were selected such that corresponding reduction degrees were approximately equivalent. The mineral phase fractions of the reduced samples were determined by X-ray diffraction (XRD) combined with Rietveld refinement.[19]

The reduction degree was defined as the ratio of oxygen removed to the initial oxygen bound to iron prior to reduction and calculated as follows. First, based on the chemical composition of the pre-reduction sample, the total iron content was calculated. The iron content in FeO was subtracted from the total Fe content, and the difference was assumed to correspond to Fe_2O_3. The total oxygen content was then calculated. Next, the weight loss measured by TG after introducing the H_2/N_2 reduction gas was assumed to arise solely from oxygen removal via iron oxide reduction, and the oxygen removed was calculated. The reduction degree was defined to reach 100% upon complete removal of the oxygen from the iron oxides.

Hematite particles (approximately 30 μm in diameter) reduced for various durations at 973 K and 1 173 K were characterized using synchrotron radiation nano X-CT and XAFS-CT. Furthermore, hematite particles from the same batch as those described above were embedded in resin and mechanically polished and sectioned for SEM and EBSD analysis.

SEM observation and EBSD mapping were performed using a ZEISS Gemini SEM 300 equipped with an Oxford Instruments Symmetry EBSD detector at an accelerating voltage of 15.0 kV. Particles from each sample were embedded in epoxy resin, mechanically ground to a flat surface using diamond paste, and finally polished with colloidal silica. A 1–2 nm thick osmium film was deposited as a conductive coating. EBSD patterns were acquired at step sizes of 0.1–0.15 μm and analyzed using "Oxford Aztec" software. Phase identification was performed considering hematite, magnetite, wüstite, and iron (α, γ) as candidate phases. An inverse pole figure (IPF) map of magnetite, along the normal direction (ND) of the measurement plane the measurement plane, was created.

Phase equilibrium calculations for the Fe–O system were performed using the thermodynamic software "*FactSage* 8.2"[20, 21] to determine the equilibrium phase assemblage corresponding to minimum Gibbs free energy for the system. Thermodynamic data for solid and liquid oxide phases were obtained from the FactSage FToxid database, while thermodynamic data for the gas phase were obtained from the FACTPS (pure substances) database. Isobaric oxygen partial pressure lines in the Fe–O system were calculated.

2.2 Synchrotron radiation nano X-CT and XAFS-CT observations

In this study, synchrotron radiation nano X-ray computed tomography (nano X-CT) and X-ray absorption fine structure computed tomography (XAFS-CT) observations were conducted using an X-ray microscope (Carl-Zeiss X-ray Microscopy Xradia Ultra) installed at the AR-NW2A beamline of PF-AR (6.5 GeV) synchrotron radiation facility at the Institute for Materials Structure Science (IMSS), High Energy Accelerator Research Organization (KEK).[13, 16] This facility focuses undulator-generated synchrotron X-rays using a condenser capillary to irradiate the sample. The transmitted X-rays is imaged by a zone plate, which acts as an objective lens. After conversion of X-rays to visible light with a scintillator, the image is enlarged and projected onto a CCD detector (12-bit, 2k×2k) with a field of view (FOV) of 20–40 μm. Spatial resolution in the projected two-dimensional images was confirmed to be better than 50 nm.

Fe_2O_3 and Fe_3O_4, both iron-based oxides, are difficult to distinguish from each other using laboratory X-ray CT with white X-rays or synchrotron nano X-CT using single-energy X-rays due to their very small density difference. Furthermore, the brightness value of each voxel is calculated as an average value. Therefore, in microstructures where fine mineral phases are heterogeneously distributed at length scales below the voxel size, this averaging effect adversely affects the accuracy of mineral phase identification and may lead to

ambiguity or misidentification. In contrast, XAFS-CT analyzes XANES spectra obtained near the absorption edge, enabling precise identification of the chemical states of target atoms within individual voxels. Consequently, this technique is highly effective for evaluating the three-dimensional distribution of Fe chemical states (Fe^{3+}, Fe^{2+}, and Fe^{0}).

In this study, XAFS-CT was performed to accurately determine the three-dimensional distribution of Fe chemical states (Fe^{3+}, Fe^{2+}, Fe^{0}) and to elucidate the hydrogen reduction behavior of hematite based on the resulting three-dimensional mineral phase distribution. The XAFS-CT observation procedure is as follows. First, three-dimensional CT images of reduced hematite particles were acquired at 28 energy points within the range of 7 090–7 200 eV near the Fe-K absorption edge. For each CT observation at a given energy, the sample was rotated from 0° to 180°, capturing 361 projection images (with an angular step of 0.5° per image). This complete XAFS-CT measurement series required approximately 8.5 hours. The acquired XAFS-CT data sets were analyzed using the X-ray microimaging analysis software "TXM-XANES Wizard"[22]. In this analysis, reconstructed images were obtained via iterative reconstruction methods after performing background correction and normalization of the CT image scaling factor at each energy. This procedure yielded a three-dimensional dataset in which each voxel was associated with an XANES spectrum. Subsequently, the XANES spectra were normalized and subjected to Linear combination fitting (LCF). LCF was performed using XANES spectra of iron oxide reference compounds and metallic iron foil as reference data. This enabled the determination of Fe valence states and quantitative phase analysis of iron-bearing species. Finally, the reduction state of the particles was evaluated based on the obtained three-dimensional distributions of Fe valence states and mineral phases.

While XAFS-CT measurements enable highly accurate determination of chemical states, they inherently require lengthy acquisition times. Therefore, for high-throughput observations, single-energy synchrotron nano X-CT was also performed. By selecting an energy near the Fe K-edge (E = 7 118.15 eV) and enhancing the absorption contrast between Fe_2O_3 and Fe_3O_4, it allows distinction between the two phases, which has been challenging with conventional X-CT. For the synchrotron nano X-CT measurements, the sample was rotated from 0° to 180° with an angular step of 0.125°, with 1 441 two-dimensional (2D) projection images acquired. The acquired images were reconstructed using filtered back-projection (FBP) to obtain three-dimensional (3D) CT images. The total scan time was approximately 60 minutes.

The 3D image data obtained from XAFS-CT and synchrotron nano X-CT were processed and visualized using Avizo Inspect (version 2022.03; Thermo Fisher Scientific Inc.) and Dragonfly (Comet Technologies Canada Inc.).

3. Results

3.1 Macroscopic reduction behavior of hematite

Figure 1 (a) shows the time dependence of the reduction degree curves of hematite at reduction temperatures of 973 K and 1 173 K (see Section 2.1 for details of the reduction degree calculation). The figure shows that the sample reduced at 1 173 K reached a reduction degree of 98% after 60 min. In contrast, the reduction of the sample at 973 K was significantly suppressed, remaining at approximately 70% after 60 min. Samples reduced for 14 min at 973 K and for 7 min at 1 173 K both exhibited reduction degrees in the range of approximately 55% to 60%.

Figures 1 (b) and 1 (c) show the mineral phase fractions determined by X-ray diffraction (XRD)-Rietveld refinement. Figure 1 (c) indicates that the 1 173 K for 60 min sample consisted of approximately 95 mass% metallic iron (Fe), with the remainder being FeO. In contrast, Fig. 1 (b) shows that the 973 K for 60 min sample exhibited a relatively low metallic iron (Fe) fraction of approximately 60 mass%, with FeO and Fe_3O_4 remaining. These mineral phase fractions are in good agreement with the trends of the reduction degree curves shown in Fig. 1 (a).

Figure 2 shows optical microscopy images of cross-sections of these reduced samples. The optical reflectance intensity of each mineral phase was highest for metallic iron, followed by Fe_2O_3, Fe_3O_4, and FeO. The observed intensity distributions confirmed that reduction proceeded inhomogeneously within each particle. Particles with a size of 10–40 μm consistently exhibited inhomogeneous internal structure under all conditions. Therefore, to investigate the reduction reaction mechanism at the tens-of-nanometers length scale, particles of approximately 30 μm, representative of the 10–40 μm size range, were arbitrarily selected for detailed analysis. Further studies are required to clarify the influence of particle size on the reduction degree.

For the selected 30 μm particles, XAFS-CT and synchrotron nano X-CT were used to systematically analyze the three-dimensional distribution of iron chemical states, mineral phases, and pores (including cracks).

3.2 Three-dimensional analysis of Fe chemical state using XAFS-CT

Three-dimensional distribution images of mineral phases (Fe_3O_4, FeO, and Fe) were created based on the three-dimensional chemical

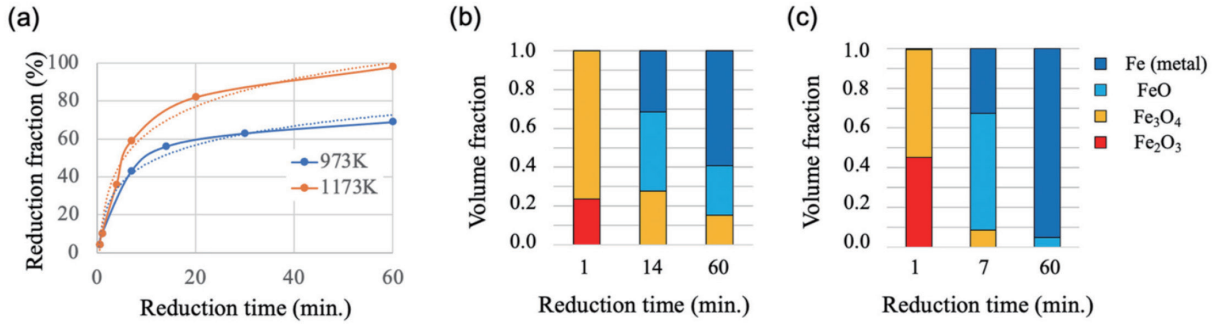

Fig. 1 (a) Changes of reduction fractions of hematite particles determined by TG.[18] (b), (c) Change of phase fractions of reduced hematite particles determined by XRD. (b) 973 K, (c) 1 173 K.[18]

state distributions of Fe derived from the analysis of XAFS-CT data. **Figures 3** and **4** show representative cross-sectional slices generated from the XAFS-CT images of the 973 K for 14 min particle and the 1 173 K for 7 min particle (red: Fe_3O_4, green: FeO, and blue: Fe). **Figure 5** displays the XANES spectra (red) and their linear combination fitting (LCF) results (blue) for regions S1–S4, extracted from the same cross-sectional phases as those shown in Figs. 3 and 4. The XANES spectra show overall good agreement with the fitting results, although minor discrepancies were observed. These discrepancies are mainly attributed to reconstruction artifacts inherent to three-dimensional volume reconstruction and to low signal-to-noise ratios (S/N), which tend to occur near complex microstructural interfaces. It should be noted that LCF analysis of XANES spectra is considered reliable when the S/N ratio exceeds approximately 500. Due to the above-mentioned effects, the phase distributions of Fe_3O_4 and Fe may be locally overemphasized near interfacial regions. Nevertheless, the identified chemical states of Fe (and the corresponding mineral phases) form continuous domains that evolve and propagate during the reduction process, reflecting diffusion-controlled reduction behavior and exhibiting physically reasonable spatial variations. These results clearly demonstrate that XAFS-CT is an effective and powerful analytical technique for elucidating the hydrogen reduction behavior of hematite.

3.3 Three-dimensional microstructural observation using synchrotron nano X-ray computed tomography

Figure 6 shows two-dimensional cross-sectional images extracted from synchrotron nano X-ray computed tomography (nano X-CT) images of 973 K for 1 min and 1 173 K for 1 min particles, acquired at multiple energies near the Fe K-edge. The cross-sectional image observed at 7 118.15 eV, approximately 7 eV above the Fe K-edge, confirmed that Fe_2O_3 and Fe_3O_4 could be distinguished

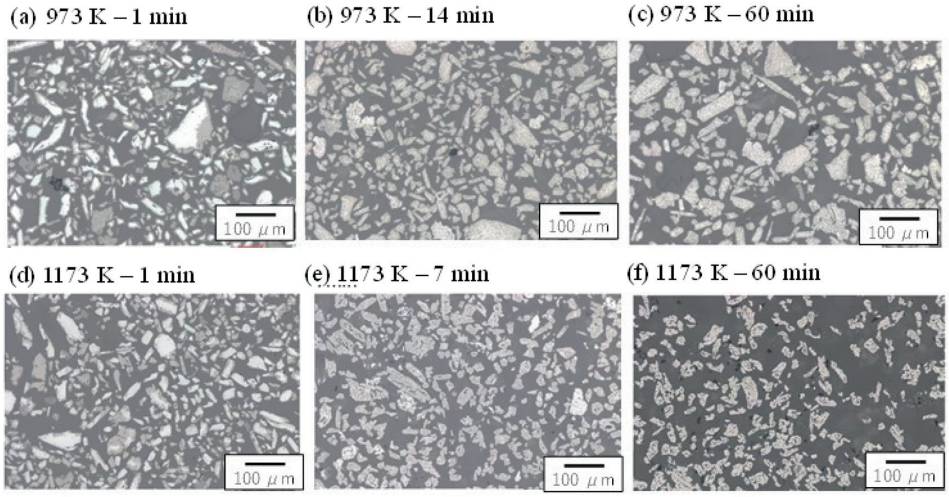

Fig. 2 Optical microscope images of reduced hematite particles: (a)–(c) 973 K and (d)–(f) 1 173 K[18)]

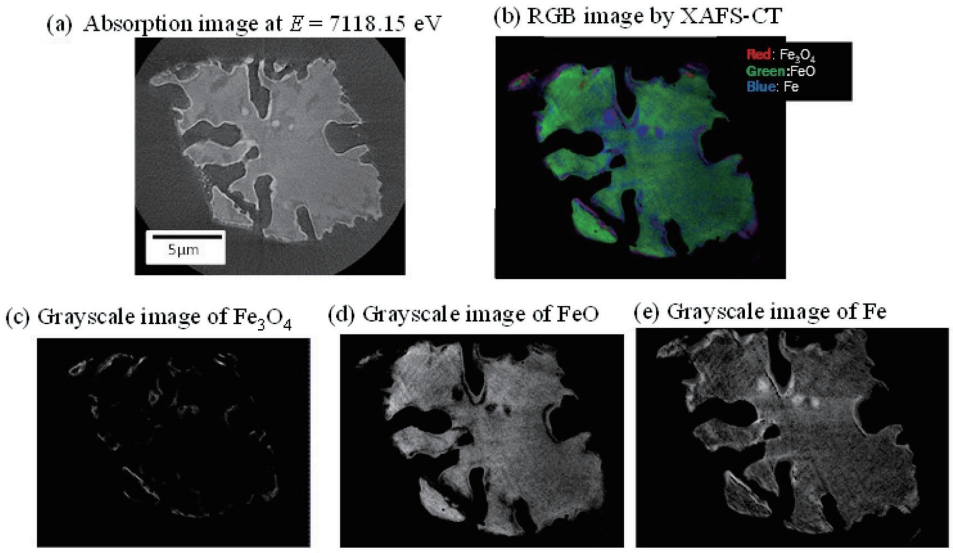

Fig. 3 Cross-sectional visualization of the mineral phase distribution of the hematite particle reduced at 973 K for 14 min, as characterized by XAFS-CT.[18)] (a) an absorption image at E = 7 118.15 eV, (b)–(e) segmented images by LCF analysis: (b) RGB-image; red: Fe_3O_4, green: FeO, blue: Fe, (c) Fe_3O_4, (d) FeO, and (e) Fe in grayscale.

more effectively. In contrast, distinguishing between the two phases was difficult in the absorption contrast images acquired at energies lower (7 047.8 eV) and higher (7 197.8 eV) than the Fe absorption edge. The densities of the iron oxide phase are Fe_2O_3: 5.27 g/cm^3 and Fe_3O_4: 5.20 g/cm^3. FeO is generally nonstoichiometric and often exists in a disordered state, with a reported density range of 5.3 to 5.7 g/cm^3. Therefore, depending on the local reduction stage (e.g., immediately following the transition from Fe_2O_3 to Fe_3O_4), the density contrast between the iron oxide phases may be extremely small, making phase discrimination based solely on density contrast difficult during reduction. However, for synchrotron nano X-ray CT images acquired at an energy (E = 7 118.15 eV) where X-ray absorption varies sensitively with the Fe valence state near the Fe absorption edge, mineral phase identification based on Fe valence becomes feasible. This clearly demonstrates that Fe_2O_3, Fe_3O_4, and FeO can be distinguished under these imaging conditions.

Figure 7 shows a representative two-dimensional cross-sectional absorption-contrast image obtained by synchrotron nano X-CT at E = 7 118.15 eV, together with the results of mineral phases and pore identification, including open and closed pores. The threshold values

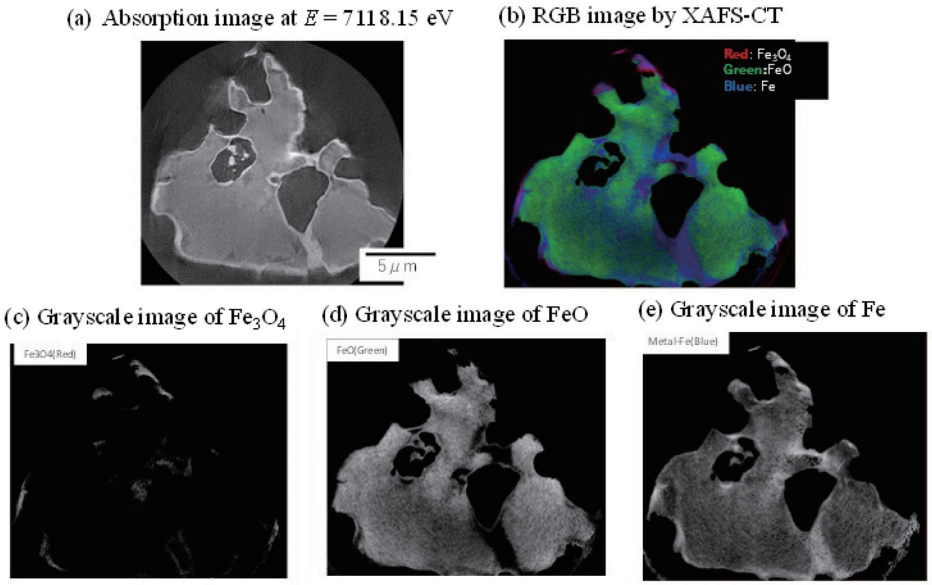

Fig. 4 Cross-sectional visualization of the mineral phase distribution of the hematite particle reduced at 1 173 K for 7 min, as characterized by XAFS-CT.[18] (a) an absorption image at E = 7 118.15 eV, (b)–(e) segmented images by LCF analysis: (b) RGB-image; red: Fe_3O_4, green: FeO, blue: Fe, (c) Fe_3O_4, (d) FeO, and (e) Fe in grayscale.

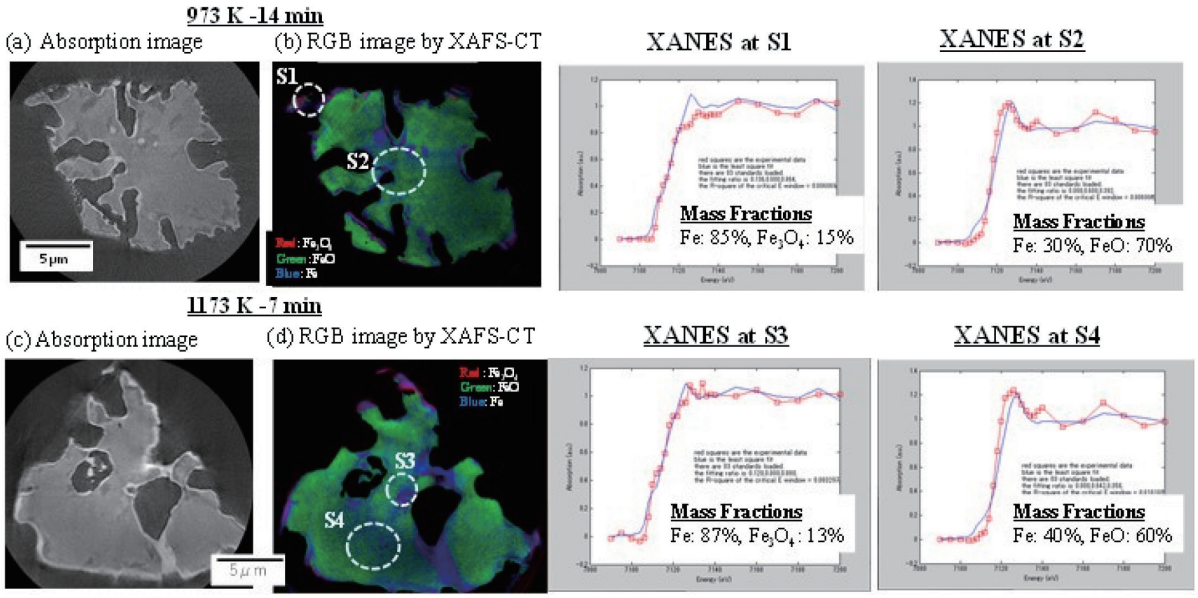

Fig. 5 Cross-sectional visualization of hematite particles reduced at 973 K for 14 min and at 1 173 K for 7 min.[18] (a), (c): CT images obtained by SR nanoscopic X-CT.[18] (b), (d): images of mineral phase distribution segmented by XAFS-CT. (XANES spectra are also shown for selected areas S1–S4.)

for mineral phase identification were determined such that the spatial distribution of the dominant phase (Fe or FeO) identified by synchrotron nano X-CT was consistent with that obtained from XAFS-CT observations. **Figure 8** shows the volume fractions of the mineral phases and pores identified in Fig. 7.

XAFS-CT measurements indicate the presence of multiple mineral phases coexisting within a single voxel ($24 \times 24 \times 24$ nm^3) (Figs. 3, 4, and 5), reflecting a gradual progression in the chemical state during reduction. In contrast, the synchrotron nano X-CT results shown in Fig. 7 represent voxel-wise averaged absorption intensities of multiple phases and pores, which precludes the discrimination of multiple mineral phases or pores within a single voxel. This fundamental difference in spatial and chemical sensitivity causes the mineral phase fractions determined by synchrotron nano X-CT to deviate from those obtained by XAFS-CT. Generally, XAFS-CT results are considered to provide more accurate representations of microstructural and chemical state information. However, the characteristic microstructure, represented by the Fe layer formed on the particle surface covering FeO, is consistently observed using both techniques.

Furthermore, synchrotron nano X-CT clearly identified the presence of Fe_3O_4 at the Fe/FeO interface. This apparent localization may be overemphasized due to the aforementioned artifact-related effects. Notably, the XRD results (Figs. 1 (b) and 1 (c)) show that the

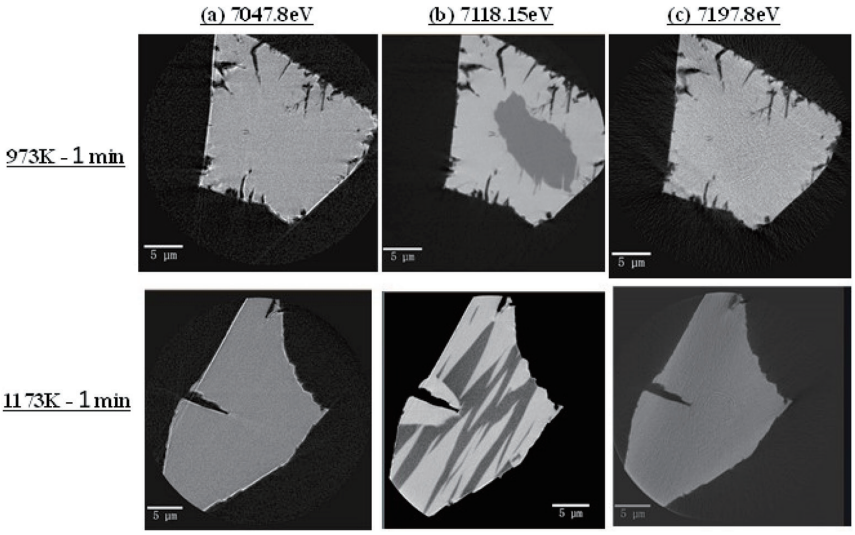

Fig. 6 Comparison of cross-sectional visualizations of the mineral phase distribution in the three-dimensional reconstructed volume data obtained by SR nanoscopic X-CT of the hematite particles reduced at 973 K for 1 min and at 1 173 K for 1 min.[18]
(a) E = 7 047.8 eV, (b) E = 7 118.15 eV, and (c) E = 7 197.8 eV.

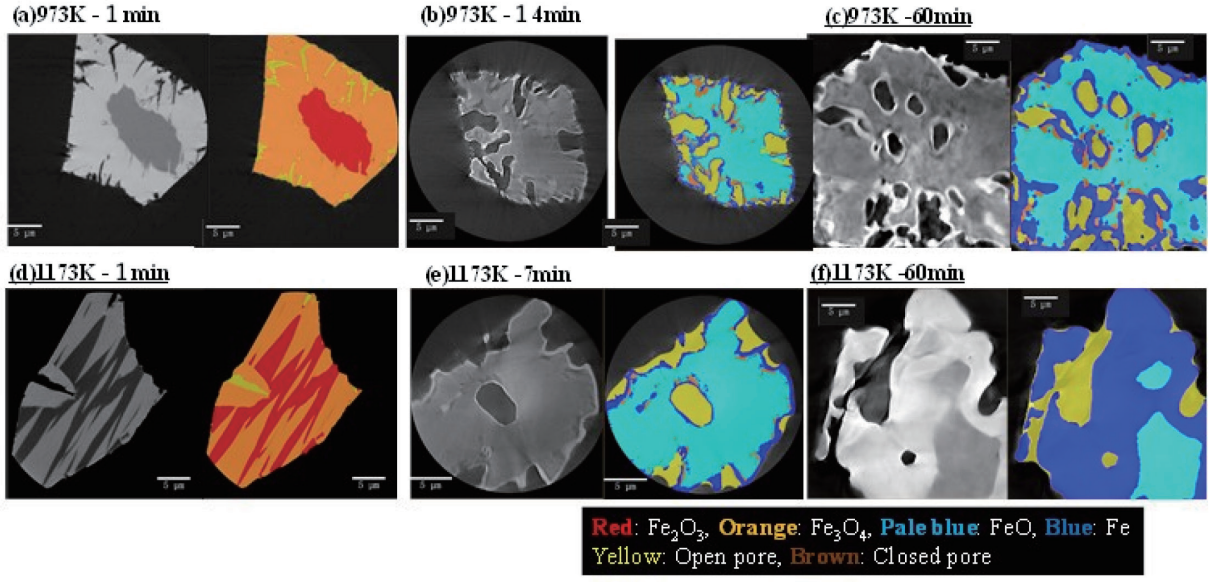

Fig. 7 CT cross-sectional visualizations of hematite particles reduced at 973 K and 1 173 K by SR nanoscopic X-CT measured at E = 7 118.15 eV, and the cross-sectional visualizations of mineral phase distribution segmented by image analysis software.[18] (a)–(c) 973 K and (d)–(f) 1 173 K: red: Fe_2O_3, orange: Fe_3O_4, pale-blue: FeO, blue: Fe, yellow: open pore, brown: close pore.

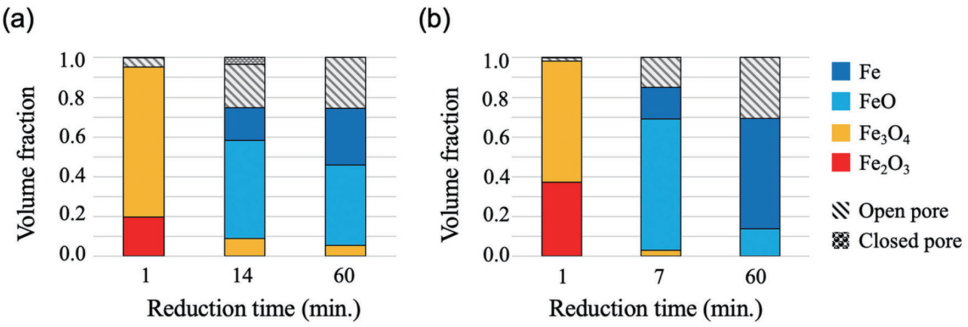

Fig. 8 Volume fractions of co-existing mineral phases and pores based on the segmented volume data determined by 3D-CT images obtained by SR nanoscopic X-CT. (a) 973 K, (b) 1 173 K.[18]

Fe_3O_4 fraction during the intermediate stage of reduction is approximately 28 mass% at 973 K and approximately 9 mass% at 1 173 K. Further detailed analyses are required to clarify the fine-scale spatial distribution of Fe_3O_4.

In light of the differences between the XAFS-CT and synchrotron nano X-CT analysis results, the following section focuses on the changes in the phase distribution.

3.4 Structural evolution of hematite particles during the reduction reaction

Using XAFS-CT and synchrotron nano X-CT, we non-destructively characterized the microstructural changes and Fe chemical states during the hydrogen reduction of iron ore particles with high spatial resolution (<50 nm) and three-dimensional spatial distribution. Based on these results, we investigated the evolution of nanostructures within hematite particles during the hydrogen reduction process.

[Early Reduction Stage]

As shown in Fig. 8, there was no significant difference in the volume fractions of mineral phases and pores between 973 K and 1 173 K during the initial stage of reduction. However, the synchrotron nano X-ray computed tomography (nano X-CT) results in Fig. 7 revealed clear differences in the spatial distribution of Fe_2O_3 between 973 K and 1 173 K. **Figure 9** shows three-dimensional reconstructions of the Fe_2O_3 regions in particles reduced at 973 K for 1 min (Fig. 9(a)) and 1 173 K for 1 min (Fig. 9(b)). At 973 K, a core–shell structure was observed, with Fe_2O_3 forming the core and being surrounded by a Fe_3O_4 shell. Cracks and pores extending from the particle surface toward the interior were observed, which are likely attributed to the volume (density) change (−1.3%) associated with the Fe_2O_3 to Fe_3O_4 transformation. In contrast, at 1 173 K, plate-like Fe_3O_4 domains were distributed throughout the entire particle.

Figure 10 shows the crystallographic orientation maps of Fe_3O_4 obtained by EBSD analysis for hematite particles reduced under the same conditions. The Fe_3O_4 domains formed at 973 K consisted of randomly oriented fine grains, whereas those formed at 1 173 K exhibited coarse, plate-like domains, whose crystal orientations were preferentially aligned, such that the (101) planes were nearly parallel to the observation plane. Previous studies have reported preferred crystallographic orientations during the reduction of Fe_2O_3 based on macroscopic microstructural analysis using XRD and EBSD.[23, 24] However, the specific orientation relationship observed in this study has not been reported previously.

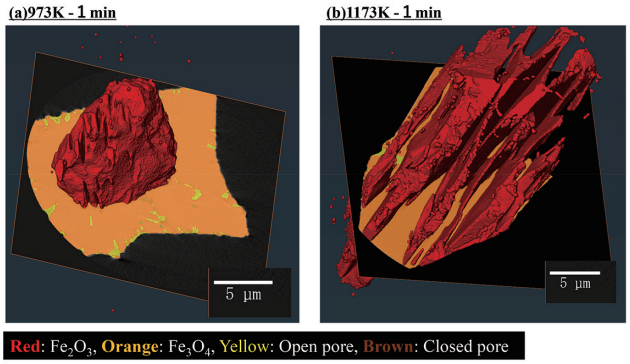

Fig. 9 Aerial perspective of the three-dimensional reconstructed volume data of the Fe_2O_3 phase obtained by SR nanoscopic X-CT measured at E = 7 118.15 eV.[18] (a) 973 K for 1 min and (b) 1 173 K for 1 min.

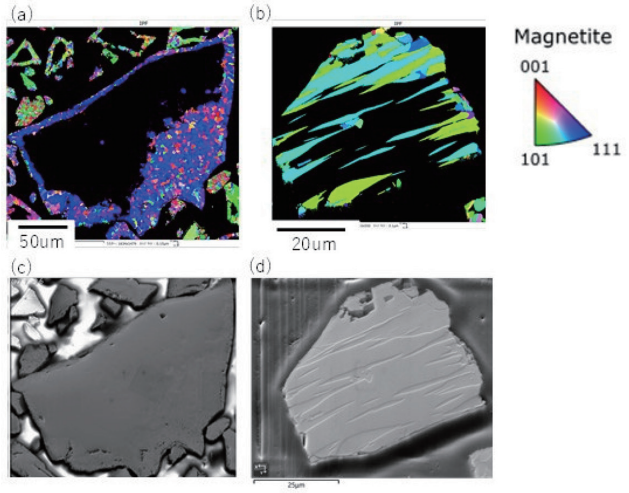

Fig. 10 (a), (b) The results of EBSD measurements and (c), (d) BSE image of the hematite particles after reduction: (a), (c) 973 K for 1 min. and (b), (d) 1 173 K for 1 min.[18]

[Mid-reduction stage]

The reduction degrees were nearly identical at 973 K for 14 min (56%) and 1 173 K for 7 min (59%) (Fig. 1(a)). The volume fractions of mineral phases in Fig. 8 also showed comparable values; however, distinct differences in the spatial distribution of mineral

phases and pores were observed (Figs. 3, 4, 5, 7). As reduction progressed, the particle morphology changed significantly. This is presumed to arise from increased surface irregularities caused by the density difference between FeO and metallic iron (Fe). Consequently, the open porosity increased markedly at both 973 K and 1 173 K. In contrast, the closed porosity remained nearly 0% under both conditions, suggesting that pore formation did not involve void generation within the interior of hematite particles, but rather originated from reduction progressing at the particle surface.

The pore structure of the 973 K for 14 min particles (Figs. 3 and 8) was more intricate and tended to exhibit smaller pore diameters compared to the 1 173 K for 7 min particles. This observation suggests that at 973 K, metallic iron forms on the particle surface by covering FeO domains, whereas at 1 173 K, metallic iron forms along plate-like domains within the particle's interior, thereby creating a microstructural environment less favorable for encapsulating FeO domains.

These results indicate that during the mid-reduction stage, the pore morphology induced by volume contraction plays a critical role in governing the microstructural progression of reduction reaction. The observed differences in pore formation are presumed to originate from distinct reaction mechanisms operative during the early reduction stage, namely topochemical reaction at 973 K and topotaxial reaction at 1 173 K.

[Late Reduction Stage]

Figure 1 (a) shows a pronounced difference in the final reduction degrees achieved at 973 K and 1 173 K. This difference, as seen in Fig. 1 (b), stems from variations in the ratios of Fe_3O_4, $Fe_{1-x}O$, and metallic iron. The 973 K for 60 min particles (Fig. 7 (c)) showed a modest increase in the thickness of the surface metallic iron layer, from approximately 0.5 μm to approximately 1 μm, compared to the 973 K for 14 min particles (Fig. 7 (b)) from the mid-reduction stage. However, the presence of residual $Fe_{1-x}O$ within the particles indicates that reduction was partially suppressed. Furthermore, this particle exhibits a fine and highly complex pore structure, which is presumed to be influenced by randomly oriented Fe_3O_4 domains formed during the early reduction stage.

On the other hand, for the 1 173 K for 60 min particles (Fig. 7 (f)), the thickness of the surface metallic iron layer exceeded 5 μm. Although a small amount of $Fe_{1-x}O$ was present within the particles, it was confirmed that reduction had progressed significantly compared to the mid-reduction 1 173 K for 7 min particles (Fig. 7 (e)). Furthermore, compared to the 973 K for 60 min particle (Fig. 7 (c)), this particle exhibited a coarse, linear pore structure. This is thought to be caused by the coarse, crystallographically oriented Fe_3O_4 domains formed during the early reduction stage.

4. Discussion

XAFS-CT enables the direct determination of the Fe chemical state and its quantitative fraction within regions of the order of several tens of nm by applying LCF to the XAFS spectral data associated with each voxel. This demonstrates the capability of XAFS-CT to determine the reduction state (Fe valence) and phase fractions with high precision. However, a notable limitation of this method is the lengthy measurement time required for data acquisition.

In contrast, synchrotron nano X-CT observations at the Fe K-edge absorption energy (7 118.15 eV) enable clear discrimination between Fe_2O_3 and Fe_3O_4, which is difficult to achieve with conventional laboratory-based X-ray CT. This approach allows rapid evaluation of samples across a wide range of reaction states, offering significantly reduced measurement times and high-throughput capability.

The differences in the nano-scale three-dimensional chemical structures within hematite observed using XAFS-CT and synchrotron nano X-CT in this study were utilized to investigate the hydrogen reduction mechanism.

During the initial reduction stage ($Fe_2O_3 \rightarrow Fe_3O_4$), Fe_3O_4 formation at 973 K proceeded uniformly from the particle surface toward the center of Fe_2O_3 particles. In contrast, at 1 173 K, Fe_3O_4 formation proceeded while preserving crystallographic relationships with adjacent Fe_2O_3 domains, as shown in Figs. 7, 9, 10.

As shown in **Fig. 11**, the reduction of hematite involves successive phase transformations accompanied by changes in the chemical state of Fe, progressing from Fe_2O_3 to Fe_3O_4, $Fe_{1-x}O$, and finally metallic Fe. The difference between 973 K and 1 173 K corresponds to variations in the oxygen concentration ranges associated with the single-phase regions of $Fe_{1-x}O$ and Fe_3O_4. From Fig. 11 (a), the oxy-

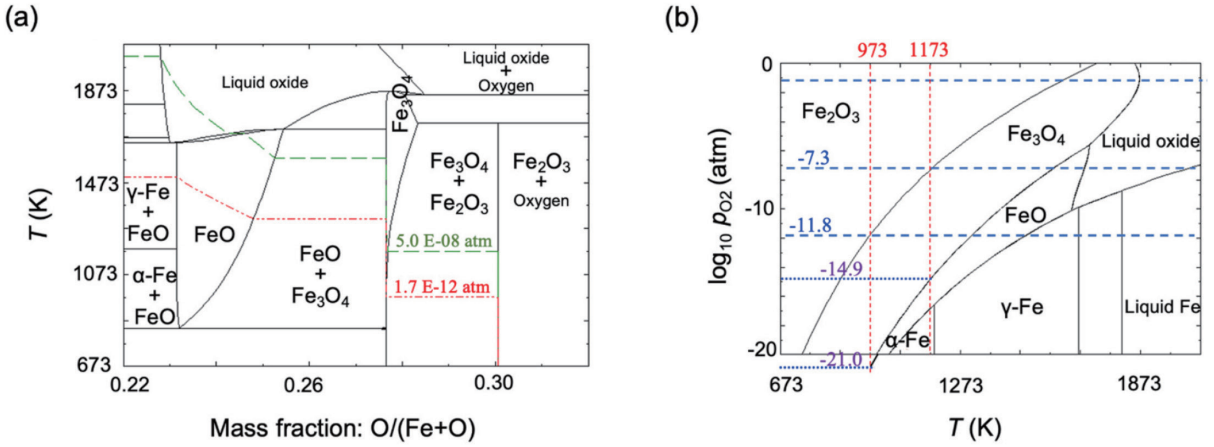

Fig. 11 Phase diagrams of the Fe-O system calculated by FactSage[18)]
(a) The temperature vs. atomic fraction: O/(Fe+O) under oxygen gas at 1 atm. (Green and red dashed lines show oxygen isobars of 5.0×10^{-8} and 1.7×10^{-12} atms, respectively.)
(b) The oxygen partial pressure ($\log_{10} pO_2$) vs. temperature. (The blue line shows the reaction conditions of experiments.)

gen concentration range for Fe_3O_4 is 0 at 973 K and 2.0×10^{-2} (mass fraction) at 1 173 K. Furthermore, the oxygen concentration range for $Fe_{1-x}O$ is 6.7×10^{-2} at 973 K and 13.3×10^{-2} at 1 173 K. In addition, from the Fe-O phase diagram shown in Fig. 11 (b), the oxygen partial pressure (pO_2) in the Fe_2O_3/Fe_3O_4 coexistence region is 1.7×10^{-12} atm at 973 K and 5.0×10^{-8} atm at 1 173 K. Since the oxygen concentration (or oxygen activity) within the Fe_2O_3 solid is expected to be significantly lower than that in air (oxygen partial pressure [pO_2] is approximately 20%), the thermodynamic difference between the two temperatures is anticipated to be even more pronounced. These density changes associated with phase transformations lead to the formation of voids and cracks, and the corresponding density (g/cm^3) variations are summarized as follows.

Fe_2O_3 (5.24 g/cm^3) → 1.3% decrease → Fe_3O_4 (5.17 g/cm^3) → 11% increase → FeO (5.74 g/cm^3) → 37% increase → Fe (7.87 g/cm^3)

By interpreting the nano-scale three-dimensional chemical and microstructural features of hematite particles discussed in Chapter 3 from a thermodynamic standpoint, the underlying reaction mechanism can be understood in terms of "topochemical" and "topotaxial" reaction pathways.

In a topochemical reaction, new phases nucleate at highly reactive regions and propagate with a sharp reaction front; thus, in this study, reduction at 973 K proceeds from the hydrogen-rich particle surface toward the particle interior. Conversely, in a topotaxial reaction, nucleation and growth of new phases occur while preserving crystallographic compatibility between the newly formed phase and the parent matrix. In this study, the Fe_3O_4 domains formed at 1 173 K grow into the particle interior while maintaining specific crystallographic orientation relationships with the Fe_2O_3 matrix.

Figure 12 shows a schematic illustration of the reaction scheme proposed for the evolution of the Fe chemical state during reduction. At the initial stage of reduction ($Fe_2O_3 \rightarrow Fe_3O_4$), reduction proceeds approximately uniformly from the particle surface toward the interior at 973 K. In contrast, at 1 173 K, Fe_3O_4 grows selectively while preserving its crystallographic relationship with Fe_2O_3 (Figs. 4 and 6). Indeed, the Fe_3O_4 regions formed at 973 K consist of fine, randomly oriented crystallites, whereas at 1 173 K, they form coarse crystalline domains preferentially oriented along {120} or {130} planes (Fig. 6). The ratio of diffusion distances at the two temperatures is estimated as exp(1 173/973) ≈ 2.3. Correspondingly, at 1 173 K, Fe_3O_4 can penetrate particles with a grain size of approximately 20 μm, whereas at 973 K, an Fe_3O_4 shell with a thickness of approximately 7–8 μm forms. This difference can be explained by the variation in the permissible oxygen concentration range within the single phase Fe_3O_4 region, as shown in Fig. 11. A narrow permissible range makes it difficult to establish a broad chemical potential gradient, thereby restricting the reaction to fine Fe_3O_4 domains. Conversely, a wide permissible range facilitates gradient formation, allowing the growth of large, crystallographically coherent Fe_3O_4 domains.

The difference in reaction schemes also influences the pore (crack) formation behavior induced by the $Fe_2O_3 \rightarrow Fe_3O_4$ phase transition. At 973 K, the topochemical reaction mechanism dominates, resulting in the formation of cracks preferentially extending along reduction diffusion paths from the particle surface toward the interior. Conversely, at 1 173 K, the topotaxial reaction mechanism prevails, leading to the formation of cracks localized along the Fe_2O_3/Fe_3O_4 interface.

Such differences in the initial reduction stage also persist into the mid-reduction phase (from Fe_3O_4 to $Fe_{1-x}O$). The permissible oxygen concentration range for the single-phase $Fe_{1-x}O$ region differs markedly between 973 K and 1 173 K (Fig. 11). At 973 K, stellate cracks form predominantly near the particle surface. For the phase transition from Fe_3O_4 to $Fe_{1-x}O$ to proceed, the oxygen concentration must decrease to near-stoichiometric levels corresponding to FeO, thereby restricting the spatial development of the $Fe_{1-x}O$ region. In contrast, at 1 173 K, cracks penetrating the particles interior along the Fe_2O_3/Fe_3O_4 interface enable access to lower oxygen concentration regimes, thereby facilitating extensive growth of $Fe_{1-x}O$ domains. Furthermore, differences in the morphology and connectivity of FeO domains formed and grown during the mid-reduction stage also strongly influence the late reduction stage ($Fe_{1-x}O \rightarrow Fe$). At this stage, the newly formed metallic iron layer acts as a diffusion barrier to hydrogen. At 973 K, the metallic iron layer encapsulated the $Fe_{1-x}O/Fe_3O_4$ regions, causing the reduction reaction to

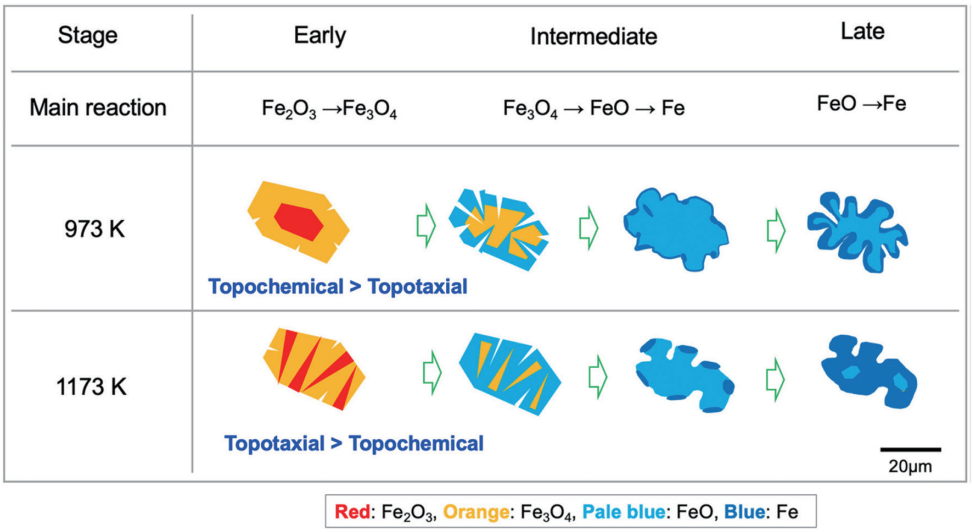

Fig. 12 Reaction schemes of reduction of Fe_2O_3 grains by hydrogen at 973 and 1 173 K[18]
Fe_2O_3 (red), Fe_3O_4 (orange), FeO (pale-blue), Fe (blue)

stall, with the reduction degree saturating at approximately 70% (Fig. 1 (a)). In contrast, at 1 173 K, the metallic iron layer forms more uniformly across grain boundaries throughout the particle, ultimately achieving a final reduction degree exceeding 95% (Fig. 1 (a)).

5. Conclusion

The combination of XAFS-CT and synchrotron nano X-CT enabled three-dimensional characterization of the heterogeneous hydrogen reduction process of hematite particles. Using XAFS-CT, the fractions of Fe_2O_3, Fe_3O_4, FeO, and metallic iron (Fe) were determined with high quantitative accuracy by applying LCF to the Fe K-edge XANES spectra assigned to each voxel. With synchrotron nano X-CT, tuning the incident X-ray energy to 7 118.15 eV enabled clear discrimination between Fe_2O_3 and Fe_3O_4, allowing high-throughput three-dimensional microstructural analysis of iron ore compared with XAFS-CT.

These techniques confirmed the existence of two distinct reduction mechanisms during the initial reduction stage: namely topochemical and topotaxial reaction, arising from subtle differences in the thermodynamic stability of Fe_2O_3, Fe_3O_4, and $Fe_{1-x}O$. It was revealed that the topochemical reaction dominates at 973 K, whereas the topotaxial reaction predominates at 1 173 K. This difference in initial reduction pathway was found to strongly influence subsequent phase transformations to Fe_3O_4, FeO, and Fe. At 973 K, a dense metallic iron layer formed on the particle surface, thereby inhibiting further reduction. In contrast, at 1 173 K, reduction proceeds more readily into the particle interior, resulting in a markedly higher final reduction degree.

Furthermore, differences in the initial reduction mechanism also lead to distinct pore and crack formation behaviors. This effect, in combination with hydrogen diffusion inhibition by the metallic iron layer, is thought to synergistically determine in the final reduction degree. These findings demonstrate that even slight differences in the thermodynamic stability of intermediate oxide phases can exert significant impact on overall reaction progress through changes in elementary reaction mechanisms, such as topochemical/topotaxial reduction. Therefore, for efficient hydrogen reduction of iron ore, it is essential not only to enhance reaction kinetics through elevated temperature and high hydrogen concentration, but also to achieve a detailed understanding of the thermodynamic relationships and accompanying nanostructure structural evolution. In this regard, synchrotron X-ray microscopy techniques, including XAFS-CT and synchrotron nano X-CT, provide powerful and indispensable tools for elucidating such mechanisms. Their application is expected to be valuable not only for iron ore reduction studies but also for a wide range of solid-gas reaction systems.

Acknowledgments

We would like to express our sincere appreciation to everyone who provided valuable technical advice and experimental assistance throughout this study. X-ray absorption spectroscopy measurements were carried out as part of a collaborative research program between Nippon Steel Corporation and the High Energy Accelerator Research Organization (Project Numbers 2021C206, 2022C206).

References

1) Zhan Du et al.: steel research int. (6), 87 (2016)
2) Sugata, M. et al.: Nihon-kinzoku-gakkaishi. 31, 574 (1967)
3) Turkdogan, E.T. et al.: Metallurgical Transaction. 2, 3175 (1971)
4) Gallegos N.G. et al.: Journal of Materials Science. 23, 451–458 (1988)
5) Kim, Se-Ho et al.: Acta Materialia. 212, 116933 (2021)
6) Wolfinger, T. et al.: Metall. Mater. Trans. B. 53B, 14–28 (2022)
7) Kimura, M. et al.: Scientific Reports. 9, 19300 (2019)
8) Watanabe, T. et al.: Composites Science and Technology. 197, 108244 (2020)
9) Kimura, M. et al.: Composites Science and Technology. 230, 109332 (2022)
10) Oshima, S. et al.: Composites Science and Technology. 257, 110837 (2024)
11) Kimura, M. et al.: J. Phys. Conf. Ser. 849, 012015 (2017)
12) Kimura, M. et al.: Sci. Rep. 8, 3553 (2018)
13) Kimura, M. et al.: The Chemical Record. 19, 1462 (2019)
14) Kimura, M. et al.: Scientific Reports. 9, 19300 (2019)
15) Takeichi, Y. et al.: Microsc. Microanal. 24 (Suppl 2), 484, (2018)
16) Niwa, Y. et al.: AIP Conference Proceedings. 2054, 050003 (2019)
17) Liu, Y. et al.: Nat. Commun. 7, Articles 12634 (2016)
18) Takayama, T. et al.: Acta Materialia. 301, 121470 (2025)
19) Takayama, T. et al.: ISIJ int. 58 (6), 1069–1078 (2018)
20) Bale, C.W. et al.: Calphad. 26 (2), 189–228 (2002)
21) Bale, C.W. et al.: Calphad. 33 (2), 295–311 (2009)
22) Liu, Y. et al.: J. Synchrotron. Radiat. 19 (2), 281–287 (2012)
23) Keeling Jr, R.O. et al.: Science. 141, 1175–1176 (1963)
24) Braga de Oliveira, F. et al.: J. Appl. Crystallogr. 53 (4), 896–903 (2020)

Toru TAKAYAMA
Senior Researcher
Materials Characterization Research Lab.
Advanced Technology Research Laboratories
20-1 Shintomi, Futtsu City, Chiba Pref. 293-8511

Masao KIMURA
Dr.Eng., Professor
Institute of Materials Structure Science,
High Energy Accelerator Research Organization (KEK)
Materials Structure Science Program,
Graduate Institute for Advanced Studies, SOKENDAI
(The Graduate University for Advanced Studies)

Yasuhiro NIWA
Ph.D., Assistant Professor
Photon Factory,
Institute of Materials Structure Science,
High Energy Accelerator Research Organization (KEK)
Materials Structure Science Program,
Graduate Institute for Advanced Studies, SOKENDAI
(The Graduate University for Advanced Studies)

Yasuo TAKEICHI
Ph.D., Associate Professor
Institute of Materials Structure Science,
High Energy Accelerator Research Organization (KEK)
Materials Structure Science Program,
Graduate Institute for Advanced Studies, SOKENDAI
(The Graduate University for Advanced Studies)

Reiko MURAO
Dr.Eng., Chief Manager, Head of Dept.
Materials Characterization Research Lab.
Advanced Technology Research Laboratories

Shoji USHIO
Ph.D, Chief Researcher, Head of Section
Ironmaking Research Lab.
Process Research Laboratories

Kazuya FUJINO
Ph.D. (Environmental Science), Researcher
Ironmaking Research Lab.
Process Research Laboratories

Takashi IIJIMA
Dr.Eng., Principal Researcher
Advanced Technology Research Laboratories